doi:10.20944/preprints202209.0308.v1

Artice

# Highly sensitive strain sensor by utilizing a tunable air reflector and the Vernier Effect

**Farhan Mumtaz [1,*], Muhammad Roman [1], Bohong Zhang [1], Lashari Ghulam Abbas [4], Muhammad Aqueel Ashraf [3], Yutang Dai [2], Jie Huang [1,**]**

[1] Department of Electrical and Computer Engineering, Missouri University of Science and Technology, Rolla, MO 65409-0040, USA.
[2] National Engineering Laboratory for Fiber Optic Sensing Technology, Wuhan University of Technology, Wuhan 430070, China.
[3] Communications Lab. Department of Electronics, Quaid-i-Azam University, Islamabad, 45320, Pakistan.
[4] Electrical Engineering Department, Sukkur IBA University, Sukkur Sindh 65200, Pakistan.
Corresponding authors: mfmawan@mst.edu (F. Mumtaz)* and jieh@mst.edu (J. Huang) **

**Abstract:** A highly sensitive strain sensor based on tunable cascaded Fabry-Perot interferometers (FPIs) is proposed and experimentally demonstrated. Cascaded FPIs consist of a sensing FPI and a reference FPI which effectively generate the Vernier Effect (VE). The sensing FPI comprises a hollow core fiber (HCF) segment sandwiched between single-mode fibers (SMFs), and the reference FPI consists of a tunable air reflector, which is constituted by a computer programable fiber holding block to adjust the desired cavity length. Simulation results predict the dispersion characteristics of modes carried by HCF. The sensor's parameters are designed corresponding to a narrow bandwidth range, i.e., 1530 nm to 1610 nm. Experimental results demonstrate that the proposed sensor exhibits optimum strain sensitivity of 23.9 pm/με in the range of 0 to 3000 με which is 13.73 times higher than the single sensing FPI strain sensitivity of 1.74 pm/με. The strain sensitivity of the sensor can be further enhanced by extending the source bandwidth. The proposed sensor exhibits ultra-low temperature sensitivity of 0.49 pm/°C in the wider temperature range of 25 °C to 135 °C, providing good isolation for eliminating cross-talk between strain and temperature. The sensor is very robust, cost-effective, easy to manufacture, repeatable, and shows a highly linear and stable response in the wider range of axial strain. Based on the sensor's performance, it may suit plenty of practical applications in the real sensing world.

**Keywords:** Vernier effect; Strain Sensor; Hollow core fiber, Fabry-Perot interferometers

## 1. Introduction

A fiber-optic strain sensor is an optical device that uses optical fiber technology to determine the strain on an object. The strain experienced by the optical fiber is measured by measuring changes in the properties of light, such as intensity, wavelength, and the state of polarization. These miniaturized sensors are based on optical fiber, which is often close to the diameter of human hair. Due to their small size, fiber-optic sensors find practical applications in compact structures and tight spaces. Fiber-optic sensors have many advantages over electrical and electronic sensors such as compact size, light weight, immunity to electromagnetic interference, low cost, stability, and high sensitivity. Due to their versatile advantages, they have been made a part of many practical applications for various industrial sectors such as defense, steel industry, structural health monitoring, civil engineering, bio-medical, and aerospace.

Fiber-optic strain sensors are reported in different designs and methodologies such as fiber Bragg grating (FBG) [1,2], long period grating (LPG) [3,4], Mach–Zehnder

Interferometer (MZI) [5–7], Michelson Interferometer (MI) [8–10], and FPI [11,12]. By exploiting the small-scale difference between the ruler and Vernier scale, the VE was originally used for high-precision length measurements. Similarly, VE can be employed to obtain ultra-high sensitive sensing structures. The optical VE is usually generated by superimposing interferograms of a reference interferometer and a sensing interferometer. Unlike conventional interferometry where the spectrum of the sensing interferometer is monitored, VE-based sensors rely on tracking shifts in the envelope of the superimposed spectrum. In optical sensing, VE-based fiber optic sensors are prominent due to their highly sensitive response to different physical quantities. VE-based FPIs are reported to attain maximum sensitivity of a fiber optic sensor for various applications, such as monitoring strain, temperature, refractive index, humidity, and pressure. Cleas *et al* [13] reported two cascaded ring resonators which work analogously to a Vernier-scale, and obtained relatively high sensitivity for refractive index measurement. The authors described the concept of VE-based sensors and presented a very detailed analysis. Liu *et al* [14] explored a high-sensitivity strain sensor based on in-fiber improved FPIs by fabricating cascaded bubbles to generate VE, and attained a strain sensitivity of 6.6 pm/με. Although their proposed sensor obtained high sensitivity, the sensor's repeatability is quite challenging due to the non-uniformity of bubbles-based air cavities. Abbas [15] reported a VE-based strain sensor and obtained optimum strain sensitivity of 37.3 pm/με but the sensor showed a limited detection range of axial strain, which was caused by the tapered structure. Nan *et al* [16] reported a VE based strain sensor with a configuration of closed air cavity with open air cavity. The proposed sensor obtained maximum strain sensitivity of 43.2 pm/με in the range of 0 to 1750 με , which is a substantial improvement in the sensor's performance in terms of sensitivity, but lateral off-setting of single mode fiber (SMF) in sensing FPI increases the risk of fragility. Andre *et al* [17] explored optical harmonic VE based strain sensor, and used a 1st, 2nd and 3rd harmonic algorithm to obtain ultra-high sensitivity of 27.6 pm/με, 93.4 pm/με and 59.6 pm/με, respectively. However. the sensor requires extra broad bandwidth to reach ultra-high sensitivity, i.e., 1200 nm to 1600 nm. Deng *et al* reported VE based strain sensor by creating in-fiber reflection mirrors using femto-second laser micromachining, and obtained strain sensitivity of 28.11 pm/με in the range of 0 to 1400 με, but such sensors require expensive equipment for fabrication. Wu *et al* [18] reported a strain sensor design using demodulation techniques of coarse wavelength and generated VE. The sensor reached a strain sensitivity of 18.36 pm/με which is substantially higher, but coarse wavelength demodulation increases the margin of error for critical applications. Zang *et al* [19] reported a highly sensitive fiber-optic sensor based on two cascaded intrinsic fiber FPIs for strain and magnetic field measurements. The sensor reached a strain sensitivity of 47.14 pm/ but showed a demerit of elongated sensing FPI and reference FPI, i.e., 9.724 mm and 9.389 mm, thus it cannot be utilized for miniaturized applications. To address the present need for industrial practical applications, still, there is a large market waiting for the development of fiber-optic sensors which have the capabilities of compactness, robustness, repeatability, stability, cost effectiveness, high sensitivity and ease of fabrications.

In this paper, a novel tunable air reflector-based strain sensor is proposed that generates an efficacious VE. The sensor has an advantageous feature of ultra-low cross-talk between strain and temperature. The isolation of the reference FPI of the sensor provides an admirable and stable response. The sensor structure is super robust and capable of measuring a large range of axial strain. Beam propagation simulation is performed to determine the excitation levels of induced modes in the interferogram. Commercially available off-the-shelf optical fibers are used to design and fabricate the proposed sensor, i.e., SMF and HCF. The sensing structure is miniaturized due to only using a few microns of the HCF segment. As the cavity length of the sensing FPI and reference FPI are accurately determined by using the computer-controlled Glass processor (GPX-3400) platform along with LDC-401 cleaver, the sensor is formed with precision. Further, a highly optimized strain sensitivity is readily obtained by using a VE subject to the limitation of the source bandwidth (i.e. 80 nm). The strain sensitivity of the proposed sensor is obtained as ~23.9 pm/με within the measurement range of 0 and 3000 με, which is 24 times higher than FBG.

The paper is organized as follows; section 2 describes working principles, section 3 demonstrates fabrication of the sensor, section 4 offers the simulated beam propagation profile of the proposed sensor, section 5 illustrates the experimental results and discussions, and finally section 6 provides a conclusion.

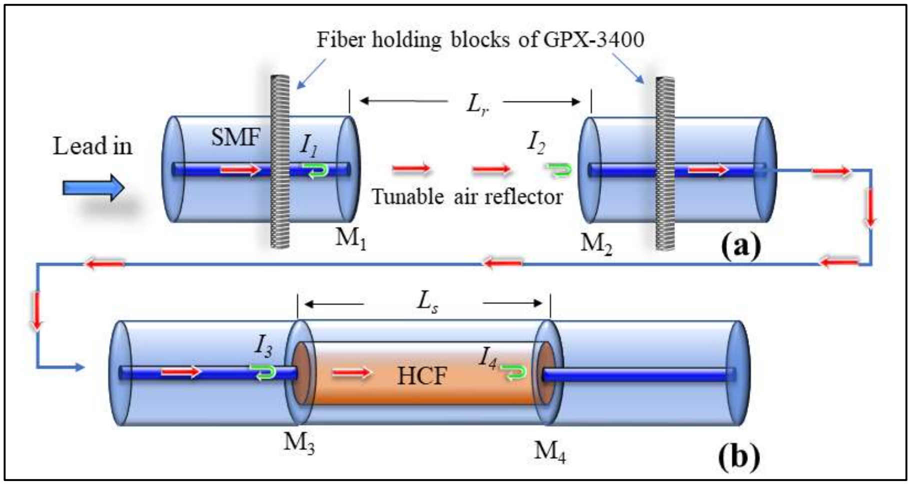

**Figure 1.** Proposed Sensor (a) Reference FPI (b) Sensing FPI.

## 2. Working Principle

The schematic of the sensing and reference FPIs are shown in Fig 1(a) and (b), respectively. To achieve the VE, the two FPIs are cascaded and the light is injected through a lead-in SMF. There are four mirrors in the proposed sensing structure, and when the light reaches the end facet of HCF (fourth mirror), the majority of light is reflected back and becomes a part of the VE interferogram, which can be expressed as,

$$I = I_1 + I_2 + I_3 + I_4 + 2\sqrt{I_1 I_2}\cos(\phi_r) + 2\sqrt{I_3 I_4}\cos(\phi_s) \quad (1)$$

Where $I_1$, $I_2$, $I_3$, and $I_4$ are the reflected light intensities from four different mirrors $M_1$, $M_2$, $M_3$, and $M_4$, respectively. $\phi_r$ and $\phi_s$ are the cosine angles measuring phase differences of the reference and sensing FPIs, and are estimated as,

$$\phi_r = \frac{4\pi n_r L_r}{\lambda}, \tag{2}$$

$$\phi_s = \frac{4\pi n_s L_s}{\lambda}, \tag{3}$$

In order to generate efficacious VE, two optical lengths are formed which are similar to each other but not equal. Thus, the cavity length of the reference and sensing FPIs can be determined as,

$$L_r = \frac{\lambda_m \lambda_{m+1}}{2n_r \lambda_m \lambda_{m+1}} \tag{4}$$

$$L_s = \frac{\lambda_k \lambda_{k+1}}{2n_s \lambda_k \lambda_{k+1}} \tag{5}$$

Where $n_r$, $n_s$ are refractive indices of reference and sensing FPI cavities. $\lambda_m$ *and* $\lambda_{m+1}$, $\lambda_k$ *and* $\lambda_{k+1}$ are the adjacent resonant dips in the wavelength interferogram of the corresponding reference and sensing FPIs, respectively. And, the wavelength of the resonant of the corresponding FPIs can be calculated as,

$$\lambda_m = \frac{4\pi n_r L_r}{2m+1}, \qquad m = 0,1,2,\ldots.. \qquad \text{for reference FPI} \tag{6}$$

$$\lambda_k = \frac{4\pi}{2k+1} n_s L_s, \qquad k = 0,1,2,\ldots.. \qquad \text{for sensing FPI} \tag{7}$$

where $L_r$ and $L_s$ are the cavity lengths of the reference and sensing FPIs, and their medium is air which assumes the refractive index: $n_r = n_s = 1$. The reference FPI is isolated, meaning only the sensing FPI will experience axial strain resulting in drifts of wavelength that can be expressed as,

$$\delta\lambda_k = \frac{4\pi \Delta L_s}{2k+1} = \frac{\lambda_k}{n_s L_s} \tag{8}$$

Above eq. (8) shows that the strain sensitivity is corresponding to the sensing FPI, and changes in cavity length due to applied strain is larger than a single FPI can sense. Free spectral range (*FSR*) of the sensing and reference FPIs can be estimated as,

$$FSR_r = \lambda_r(m-1) - \lambda_r(m) = \frac{\lambda_r^2}{2n_r L_r} \tag{9}$$

$$FSR_s = \lambda_s(k-1) - \lambda_k(k) = \frac{\lambda_s^2}{2n_s L_s} \tag{10}$$

According to VE theory, the envelope $FSR_e$ can be estimated as,

$$FSR_e = \left| \frac{FSR_s \bullet FSR_r}{FSR_s - FSR_r} \right| \tag{11}$$

By employing VE, the sensor's sensitivity can be substantially improved by tracking the drift of the envelope depression. Thus, an amplification factor *M* of the VE-satisfying sensor can be estimated as,

$$M = \frac{FSR_s}{FSR_r - FSR_s} \tag{12}$$

and drift in wavelength of the envelope can be expressed as,

$$\delta\lambda_e = M \times \delta\lambda_k = \frac{FSR_s}{FSR_r - FSR_s} \times \frac{\lambda_k}{L_s} \Delta L_s \tag{13}$$

From eq. (13), it can be inferred that VE phenomena can substantially enhance the sensitivity of the sensor by M times. Thus, the proposed sensor will be able to measure axial strain with high sensitivity by employing VE in the sensing structure.

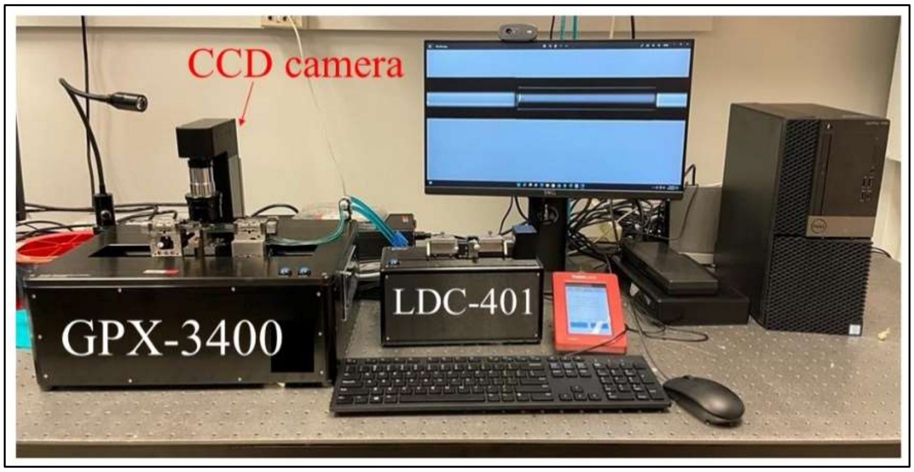

**Figure 2.** Splicing and cleaving setup for the fabrication of the proposed sensor.

## 3. Fabrication of the Sensor

The proposed sensor is designed with two different FPIs. The reference FPI consists of HCF, and the sensing FPI consists of a HCF sandwiched between SMFs. A SMF-28e with core and cladding diameter of 8.2 μm and 125 μm, respectively, is used as a lead-in fiber. A HCF, with inner and outer diameter of 55.1 μm and 125 μm, respectively, is used to fabricate the sensing FPI. The sensor is fabricated by a simple process of splicing and cleaving. The GPX-3400 and LDC-401 cleaver are used in the fabrication of the proposed sensor, as shown in Fig. 2. The fabrication process is as follows: Sensing FPI is formed by splicing of SMF-HCF-SMF in the form of concatenation. The SMF is cleaved and then spliced with a piece of HCF, as shown in Fig. 2(a-b). Then, the HCF is cleaved at 400 μm with the LDC-401 cleaver which has the ability to cleave at a micro-scale with high precision. After cleaving the HCF, it is spliced with SMF, so that SMF-HCF-SMF structure is formed. The GPX-3400 is a computer-aided device that provides high precision while splicing of optical fibers, and the splicing is performed with controlled filament burning. The SMF and HCF are spliced with filament power of ~70W, a pre-gap distance of 8.0 μm, a pre-push distance of 5.0 μm, a hot push distance of 14.0 μm, and a filament burning duration of 5 sec. The reason for using low power while splicing the HCF with SMF is that HCF has a hollow air core, and if high power is used for splicing the HCF collapses and subsequently deforms the fiber shape. The reference FPI is formed by placing a cleaved SMF fiber on the GPX-3400 fiber holding blocks. The fiber holding blocks of the GPX-3400 platform are computer-controlled, which helps to align the fibers. The reference FPI is a tunable air reflector that can be adjusted. In order to examine the sensor's performance corresponding to VE, three different samples of air reflectors are tuned to form reference FPIs, i.e., S-1 = 375 μm, S-2 = 365 μm, and S-3 = 355 μm. The schematic fabrication process of the proposed sensor is shown in Fig. 3. The microscopic images of longitudinal cross-sections of tunable reference FPIs, the sensing FPI, and the transverse cross-sections of SMF & HCF are shown in Fig. 4(a-d), respectively. Microscopic images are taken by GPX-3400 which has a CCD camera connected to the computer as shown in Fig. 2.

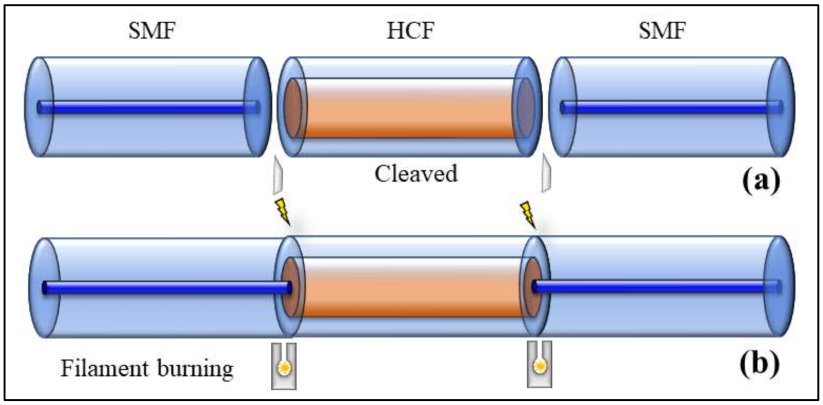

**Figure 3.** Fabrication process of Sensing FPI

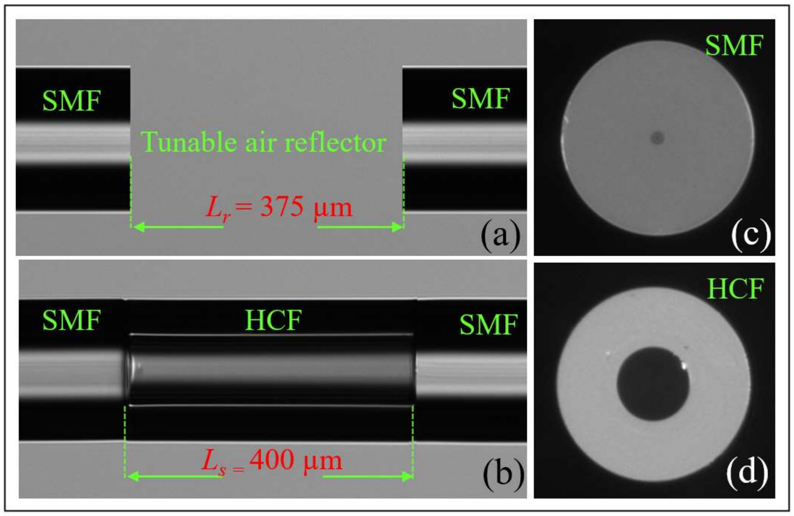

**Figure 4.** Microscopic images of the proposed sensor (a) longitudinal cross-section of (a) tunable reference FPI (b) sensing FPI, and transverse cross-section of (c) SMF (d) HCF.

## 4. BPM profile of the Sensor

In order to further analyze the light beam propagation in the proposed sensing FPI, a 3-dimensional beam propagation module (BPM) is used by Rsoft software. Fig. 5(a) demonstrates the slice view of beam propagation in the *xz*-plane for the sensing FPI, where yellow and grey colors depict the SMF and HCF, and their parameters are consistent with the original datasheets of the optical fibers. Fig. 5(b) describes the modal profile of beam in the *xz*-plane which is propagated through SMF-HCF-SMF. The inset of Fig. 5(b) depicts the *xy*-mode profile propagating through the deployed optical fibers corresponding to the z-direction. Crossection "A" is taken at z = 10 µm, specifying the fundamental mode profile with an effective mode index of 1.46326 which is injected via lead-in SMF. Crossection "B" is taken at z = 300 µm, which shows the $E_x$ mode profile with an effective mode index of 1.465242 at the middle of HCF, and it can be observed that light started spreading via the hollow core to the cladding region. Crossection "C" is taken at z = 500 µm where the beam of light exits the HCF segment. The light is further dispersed into the cladding region and obtains a higher order (HE) mode with effective mode index 1.466397. Finally, cross-section "D" is taken at z = 900 µm with an effective mode index of 1.46675. It can be seen that the light intensity further deteriorates while exiting from the HCF due to the air reflector. At this point, HE modes are more prominent. Fig. 5(c) displays the light intensity profile of the light beam which is injected through the lead-in SMF. The profile provides a better understanding of the intensity of light distribution as it propagates through the sensing structure. Consequently, a major portion of the light is reflected from the cross-section "C" region and becomes part of the interferogram. Fig. 5(d) provides a 3-dimensional view of the modal profile for the proposed sensing structure which further classifies the mode dispersions while the light beam is exiting from HCF and eventually excites HE modes.

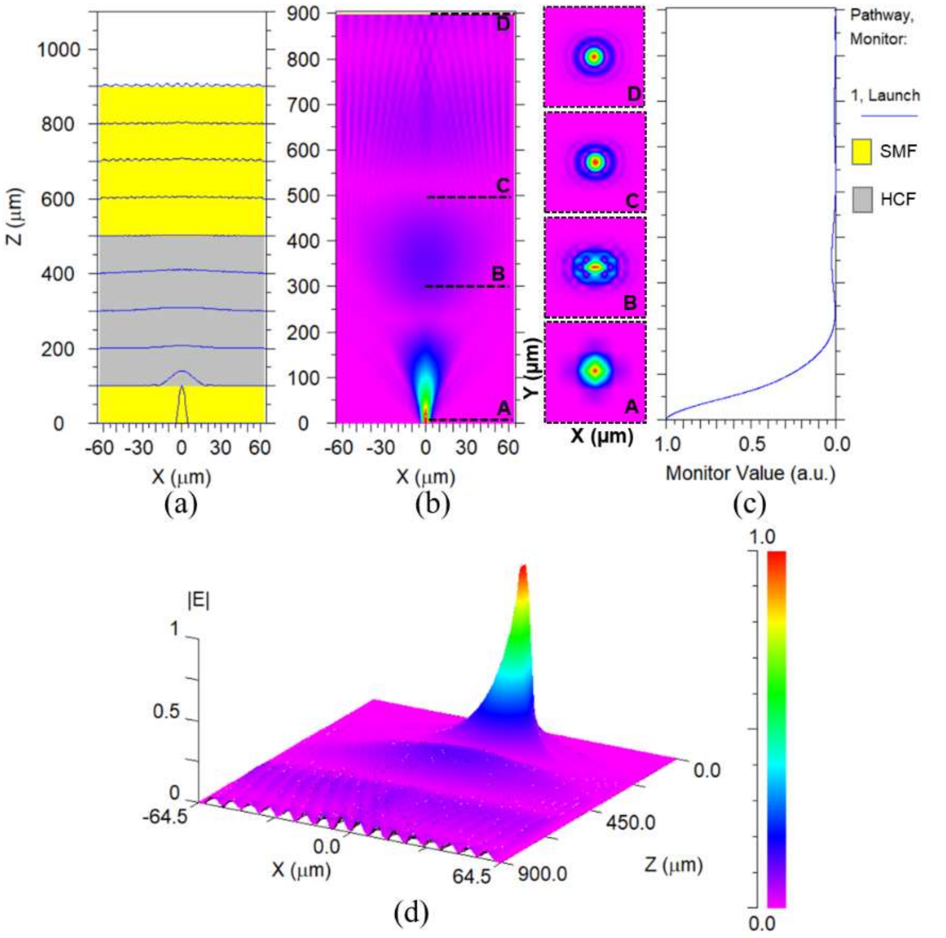

**Figure 5.** BPM profile of the proposed sensor (a) Slice view in the *xz*-plane (b) modal profile in the *xz*-plane and insets show the *xy*-plane mode field at different z, (c) Monitor pathway of light intensity propagating through the sensor, and (d) 3-dimensional mode field distribution.

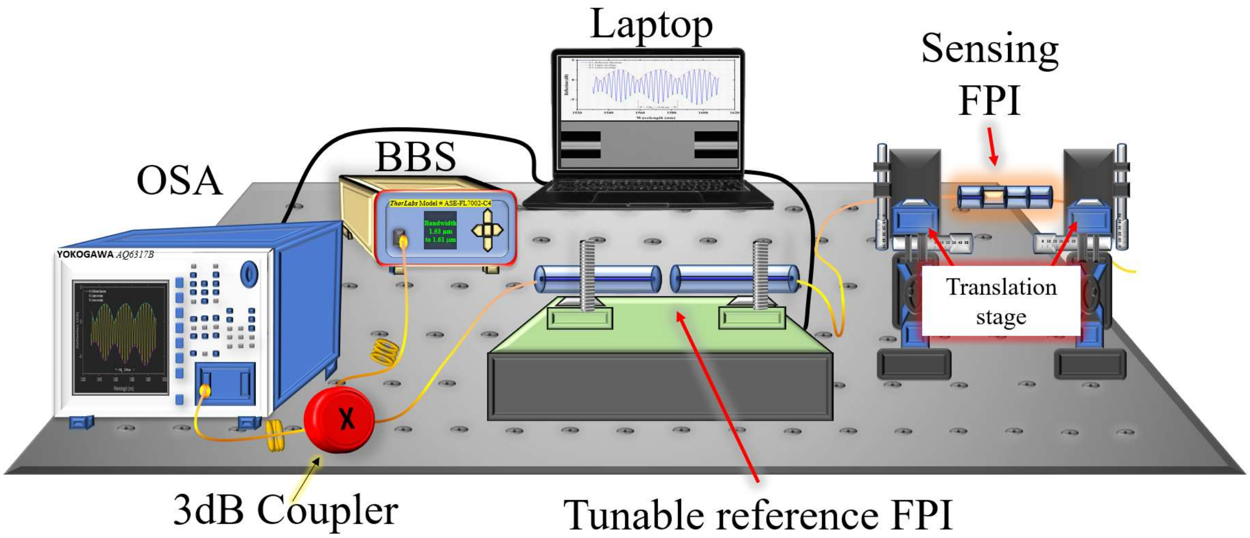

**Figure 6.** Schematic experimental setup for strain measurements.

## 5. Experimental Results and Discussions

A schematic of the experimental setup for the axial strain measurement is shown in Fig. 6. A broadband source (Thorlabs, Model # ASE-FL7002-C4) with a narrow bandwidth of 1530 nm to 1610 nm, optical spectrum analyzer (Model # AQ6317B), a laptop for the acquisition of data, and a 3dB coupler are used to obtain the reflection spectrum of the proposed sensor. For reference, axial strain measurements were taken with the sensing FPI structure, without the cascading tunable reference FPI. The sensing FPI response to different values of axial strain from 0 to 3000 $\mu\varepsilon$ are recorded and plotted as wavelength shift vs applied axial strain, as shown in Fig. 7. The FSR of the sensing FPI was obtained as 2.985 nm whereas the strain sensitivity of a single sensing FPI is obtained as 1.74 pm/$\mu\varepsilon$ with excellent linear fit correlation. The inset of Fig. 7 depicts the spectrum evolution of the sensing FPI dip, which shifts linearly with the increasing value of axial strain.

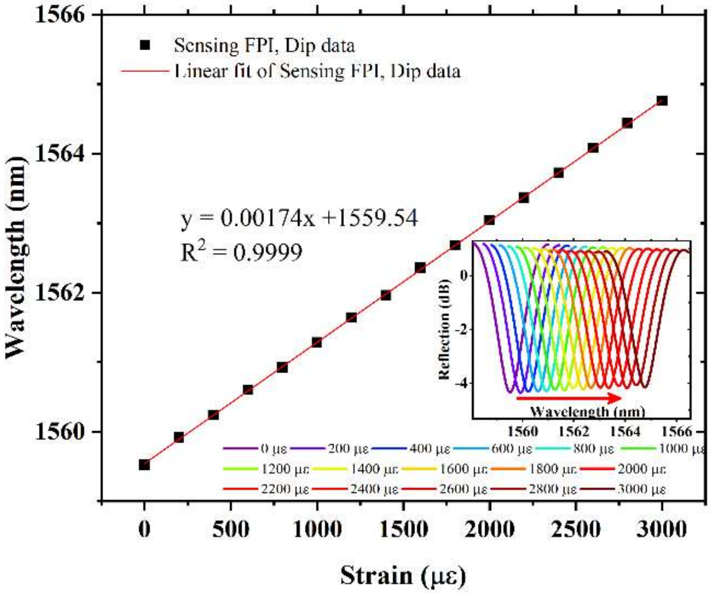

**Figure 7.** Axial strain measurement response of single sensing FPI.

Thereafter, to realize the VE of the proposed sensor, the sensing FPI was cascaded with the tunable reference FPI. Three different samples of tunable reference FPIs were used to analyze the VE of the proposed sensor, i.e., S-1, S-2, and S-3. Fig. 8 depicts the reflection interference spectrum of S-1, S-2, and S-3. The curve fitting method was used to draw the upper and lower envelopes over the VE interference pattern. The measured envelope $FSR_e$ of S-1, S-2, and S-3 are 41.45 nm, 31.33 nm, and 24.96 nm as shown in Fig. 8 (a-c), which are consistent with theoretically calculated values as, 41.74 nm, 30.97 nm, and 24.62 nm, respectively.

doi:10.20944/preprints202209.0308.v1

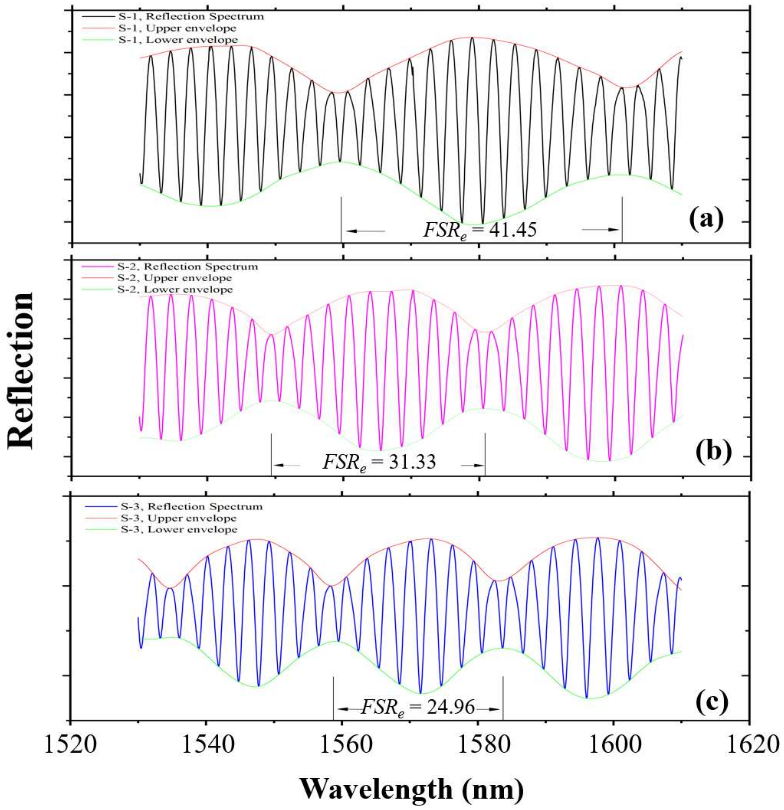

**Figure 8.** $FSR_e$ of cascaded FPIs (a) S-1 (b) S-2 (c) S-3.

The axial strain response of S-1 is measured by using the experimental setup as shown in Fig. 6. The spectral evolution of S-1 is recorded by applying stress, which causes axial strain from 0 με to 2600 με with an axial strain step of 200 με. The envelope dip produces a red shift in the spectra corresponding to increasing axial strain. The wavelength vs envelope data of S-1 is plotted in Fig. 9. It can be seen that by using VE, S-1 strain sensitivity is 23.9 pm/με, which is almost 14 times higher than that of a single sensing FPI. The S-1 measurement also provides an excellent linear fit correlation function with $R^2$ = 0.99751. The measured strain values match well with theoretical analysis, and a small error is seen which is induced by equipment measurement error. Further, in order to realize the amplification factor of the proposed sensor, different cavity lengths in the cascaded FPIs are tested, i.e., S-2 and S-3. Air cavities for the reference FPIs are formed using a tunable cavity platform, where the cavity lengths for S-2 and S-3 are 365 μm and 355 μm, respectively. The FSR of the individual reference FPIs for S-2 and S-3 is measured as 3.28 nm and 3.36 nm, respectively. The spectral evolution is presented in the inset of Fig. 10. S-2 exhibits axial strain sensitivity of 17.54 pm/με with an excellent linear correlation function of $R^2$ = 0.99905 in the strain measurement range of 0 με to 3000 με, and produces a red-shift with increasing axial strain, as shown in Fig. 10. The strain sensitivity of S-2 is 10 times higher than that of the single sensing FPI. Finally, S-3 was tested for measuring its response to axial strain. Like S-1 and S-2, S-3 also produced a red-shift in the spectral evolution with increasing axial strain. The plot of S-3 exhibited wavelength vs dip variation due to axial strain is shown in Fig. 11. S-3 exhibits axial strain sensitivity of 14.11 pm/με which is 7.98 times higher than the single sensing FPI, and shows an excellent linear correlation function of $R^2$ = 0.999 in the strain measurement range of 0 με to 3000 με, as shown in Fig. 11.

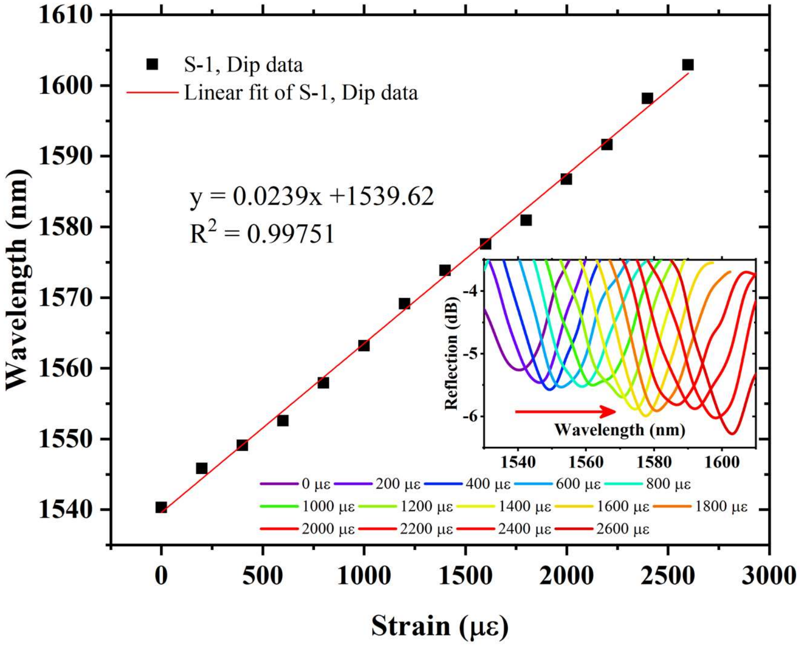

**Figure 9.** Sensitivity and linear correlation function of S-1, and inset exhibits spectral evolution of envelope dip data.

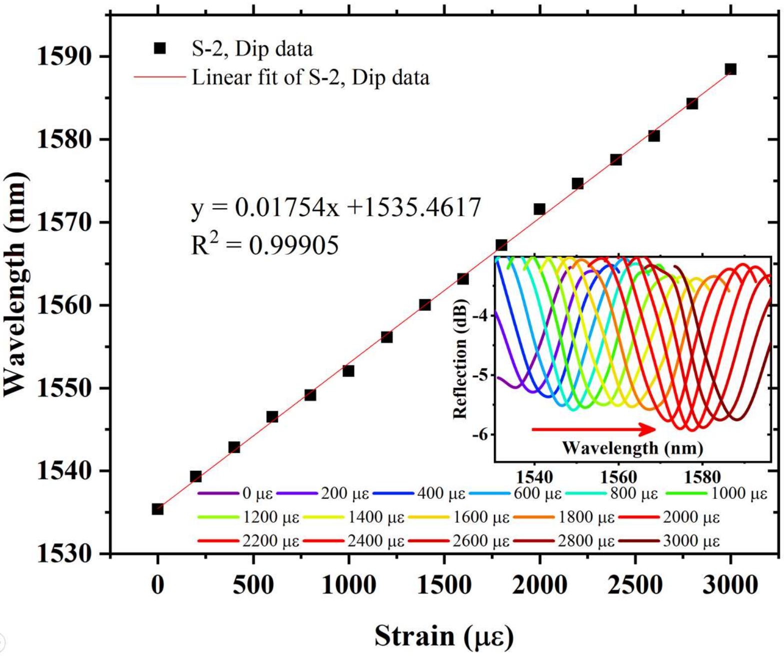

**Figure 10.** Sensitivity and linear correlation function of S-2, and inset exhibits spectral evolution of envelope dip data.

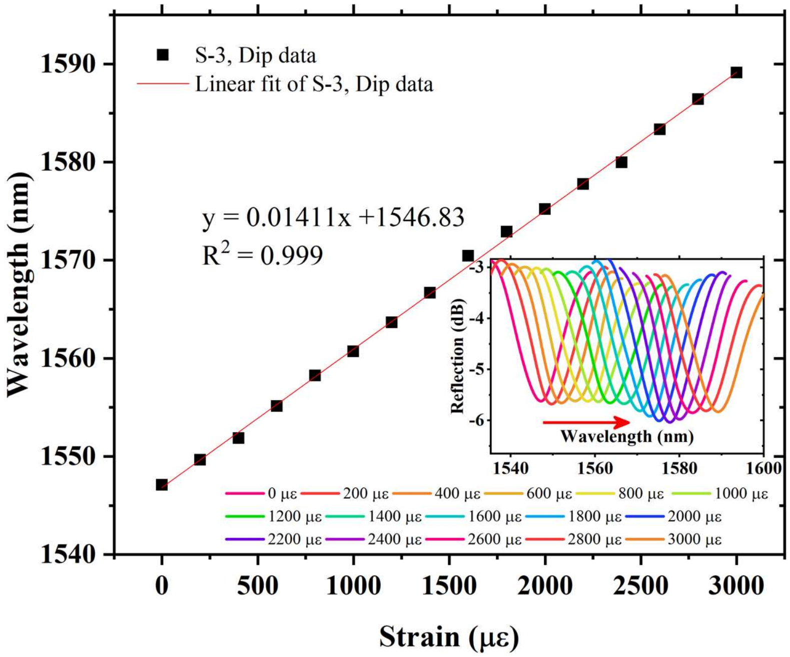

**Figure 11.** Sensitivity and linear correlation function of S-3, and inset exhibits spectral evolution of envelope dip data.

It can be inferred that by reducing the cavity length of the reference FPIs of S-1, S-2, and S-3, the $FSR_e$ of each sample is reduced and exhibits a substantial decrease in strain sensitivity. S-1 reached maximum sensitivity of 23.9 pm/με subjected to the limitation of source bandwidth, i.e., 80 nm. However, the strain sensitivity of the sensor can be further enhanced by increasing the bandwidth of the source. Nevertheless, the proposed sensor showed a highly sensitive response to strain and provided measurements over a wider range of axial strain by employing a narrow bandwidth of source which is an advantageous feature of the sensor, and the wider range of strain measurement confirms that it is a mechanical robust sensing structure. The length of the sensor's structure is 800 microns, which further confirms its compactness. The obtained sensitivity and *FSR's* of the three samples are listed in Table 1.

**Table 1.** *FSR* and sensitivity of the proposed sensor

| **Sample** | $FSR_r$ **(nm)** | $FSR_s$ **(nm)** | $FSR_r$ **(nm)** | **Magnification factor M** | **Sensitivity (pm/με)** |
|---|---|---|---|---|---|
| S-1 | 3.20 | 2.985 | 41.45 | 13.73 | 23.9 |
| S-2 | 3.28 | 2.985 | 31.33 | 10.08 | 17.54 |
| S-3 | 3.36 | 2.985 | 24.96 | 7.98 | 14.11 |

The repeatability of the sensor is also tested after taking the strain measurements. Fig. 12 exhibits the repeatability of the sensor. The up-strain measurements were taken in the strain measurement range of 0 με to 3000 με, and which were then followed by down-strain measurements over the same range. It is observed from both up and down-strain measurements that the envelope dips of three samples are very stable and approximately return to the same position, however, a very small fluctuation is observed in linearity which is negligible and is caused by the strain measurement error of equipment. A comparison of the proposed sensor is made with earlier reported sensors which is listed in Table 2. It can be ascertained from the comparison that an effective use of VE in sensing architecture can significantly enhance the sensitivity of the sensor, and the proposed sensor demonstrated higher sensitivity with a wider strain detection range.

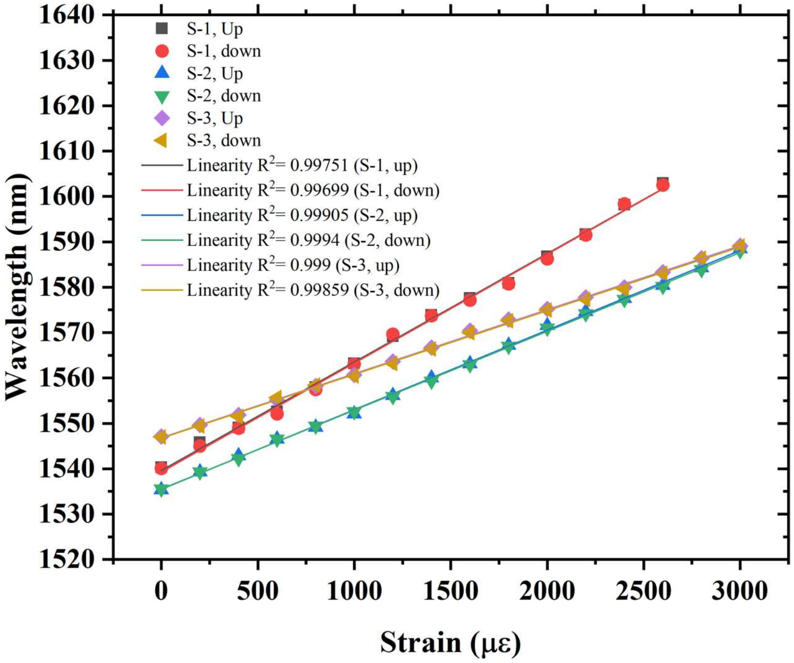

**Figure 12.** Repeatability test of the proposed sensor.

**Table 2.** Comparison of the proposed sensor with earlier reported sensors

| Reference | Sensing Structure | Strain sensitivity (pm/ με) | Strain measurement Range (με) | Temperature sensitivity (pm/°C) | Temperature measurement range (°C) |
|---|---|---|---|---|---|
| [2] | FBG | 1.14 | 0 – 5000 | 11.2 | 25 – 200 |
| [3] | PCF LPG | -7.6 | 0 – 800 | 3.91 | 20 – 90 |
| [4] | LPG | 4.37 | 0 – 700 | 85.0 | 0 – 60 |
| [6] | MZI | 1.19 | 0 – 800 | 137.6 | 20 – 90 |
| [7] | MZI with Microcavity | 6.8 | 0 – 700 | - | - |
| [10] | Hybrid | 11.6 | 0 – 295 | 11.6 | 30 – 210 |
| [12] | Micro-FPI | 2.39 | 0-9800 | 0.9 | 30 – 100 |
| [14] | Bubble bases FPI | 6.0 | 0 – 1000 | 1.1 | 100 – 600 |
| [15] | Tapered + Cascaded FPIs | 37.3 | 0 – 444.4 | 0.7 | 30 – 80 |
| [19] | Cascaded FPIs | 47.14 | 0 – 60 | - | - |
| This work | Tunable Cascaded FPIs | 23.9 | 0 – 3000 | 0.49 | 25 – 135 |

Temperature response of the proposed sensor was also tested. In order to test the temperature response, the sensing FPI is placed into a heating furnace whose temperature error is about 0.1 °C. The temperature measurements were recorded from 25 °C to 135 °C with a temperature step of 10 °C as shown in Fig. 13. The sensor exhibits ultra-low temperature sensitivity of 0.49 pm/°C with a good linear correlation function of $R^2$ = 0.9982, as shown in Fig. 14. The low sensitivity of the sensing FPI cannot be further amplified with VE because both have nearly identical cavities and wouldn't influence a large change in refractive index when exposed to an analogous temperature environment. Therefore, ultra-low temperature sensitivity is a superior aspect of the proposed sensor which helps to eliminate the temperature cross-talk with strain measurements. The proposed sensor exhibits temperature crosstalk corresponding to strain as low as 0.0205 με/°C. This shows that the proposed sensor is fully capable of compensating for temperature variations when it is under different strains. Thus, the cascaded FPIs sensing structure with VE has many advantages for numerous practical applications.

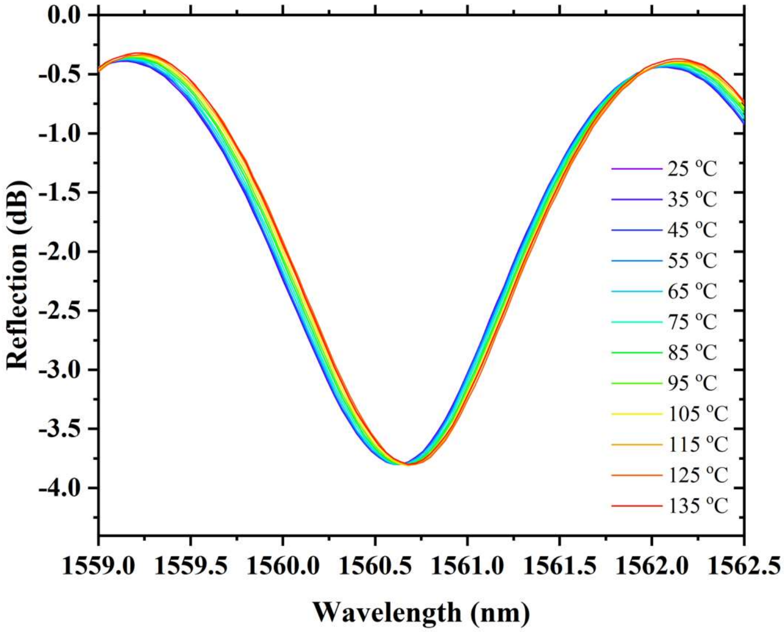

**Figure 13.** Spectral evolution of the proposed sensor with temperature rise.

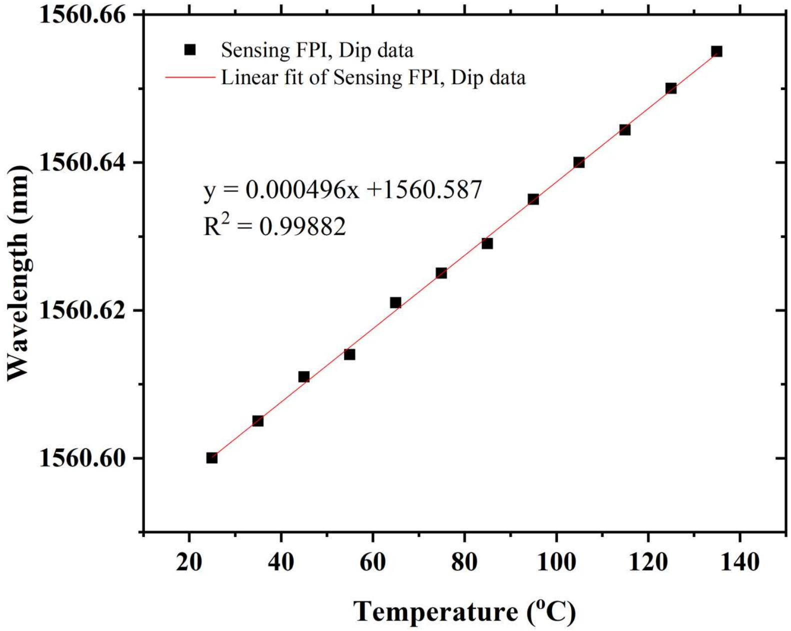

**Figure 14.** Sensitivity and linear correlation function.

## 6. Conclusions

In summary, a highly sensitive strain sensor based on tunable cascaded FPIs is experimentally demonstrated. Cascaded FPIs efficaciously generate the Vernier Effect in the sensing structure. The novelty of the sensor is to tune a desired air reflector cavity for the reference FPI to obtain higher sensitivity and improve performance. The Vernier Effect enhances the sensor's sensitivity 13.73 times that of a single sensing FPI. The robustness of the sensor enables the measurements of large strains. The sensor is designed for narrow bandwidth sources in a flexible manner and presents low crosstalk with temperature, as low as 0.0205 με/°C. The advantageous features of the proposed sensor are easy fabrication, cost-effectiveness, high sensitivity, mechanical robustness, repeatability, compactness, and precise control of the FPI's cavity, which makes it suitable for numerous industrial applications.

**Author Contributions:** Conceptualization, methodology, simulations, writing—original draft preparation, visualization, experimental investigation, project administration, F. Mumtaz; experimental investigation, writing—review and editing, M. Roman; experimental investigation, writing—review and editing, B. Zhang; validation, methodology, L.G. Abbas, writing—review and editing, supervision M.A. Ashraf; visualization, supervision, Y. Dai; supervision, project administration, funding acquisition, review and editing, J. Huang. All authors have read and agreed to the published version of the manuscript.

**Funding:** This work was supported by a research grant of the Missouri University of Science and Technology, Rolla, 65401-0040, Rolla, USA in a Post-doc fellowship program for F. Mumtaz.

**Acknowledgments:** J. Huang is grateful for support from the Roy A. Wilkens Professorship.

Endowment, Missouri S&T, Rolla, 65409-0040, USA

**Conflicts of Interest:** The authors declare no conflict of interest

**Institutional Review Board Statement:** Not applicable.

**Informed Consent Statement:** Not applicable.

**Data Availability Statement:** Not applicable.

## References

1. Sahota, J.K.; Gupta, N.; Dhawan, D. Fiber Bragg Grating Sensors for Monitoring of Physical Parameters: A Comprehensive Review. *Opt. Eng.* **2020**, *59*, 1, doi:10.1117/1.oe.59.6.060901.
2. Liu, N.; Li, Y.; Wang, Y.; Wang, H.; Liang, W.; Lu, P. Bending Insensitive Sensors for Strain and Temperature Measurements with Bragg Gratings in Bragg Fibers. *Opt. Express* **2011**, *19*, 13880, doi:10.1364/oe.19.013880.
3. Wang, Y.-P.; Xiao, L.; Wang, D.N.; Jin, W. Highly Sensitive Long-Period Fiber-Grating Strain Sensor with Low Temperature Sensitivity. *Opt. Lett.* **2006**, *31*, 3414, doi:10.1364/ol.31.003414.
4. Zhou, D.P.; Wei, L.; Liu, W.K.; Lit, J.W.Y. Simultaneous Measurement of Strain and Temperature Based on a Fiber Bragg Grating Combined with a High-Birefringence Fiber Loop Mirror. *Opt. Commun.* **2008**, *281*, 4640–4643, doi:10.1016/j.optcom.2008.06.001.
5. Lu, P.; Chen, Q. Asymmetrical Fiber Machzehnder Interferometer for Simultaneous Measurement of Axial Strain and Temperature. *IEEE Photonics J.* **2010**, *2*, 942–953, doi:10.1109/JPHOT.2010.2082513.
6. Mumtaz, F.; Lin, H.; Dai, Y.; Hu, W.; Ashraf, M.A.; Abbas, L.G.; Cheng, S.; Cheng, P. Simultaneous Measurement of Temperature and Strain Using Multi-Core Fiber with in-Line Cascaded Symmetrical Ellipsoidal Fiber Balls-Based Mach-Zehnder Interferometer Structure. *Prog. Electromagn. Res. C* **2021**, *112*, 21–34, doi:10.2528/PIERC21021002.
7. Liao, C.R.; Wang, D.N.; Wang, Y. Microfiber In-Line Mach–Zehnder Interferometer for Strain Sensing. *Opt. Lett.* **2013**, *38*, 757, doi:10.1364/ol.38.000757.
8. Miliou, A. In-Fiber Interferometric-Based Sensors: Overview and Recent Advances. *Photonics* **2021**, *8*, doi:10.3390/photonics8070265.
9. Hua, L.; Song, Y.; Huang, J.; Lan, X.; Li, Y.; Xiao, H. Microwave Interrogated Large Core Fused Silica Fiber Michelson Interferometer for Strain Sensing. *Appl. Opt.* **2015**, *54*, 7181, doi:10.1364/ao.54.007181.
10. Abbas, L.G.; Ai, Z.; Mumtaz, F.; Muhammad, A.; Dai, Y.; Parveen, R. Temperature and Strain Sensing with Hybrid Interferometer. *IEEE Sens. J.* **2021**, *21*, 26785–26792, doi:10.1109/JSEN.2021.3120798.
11. Ma, Z.; Cheng, S.; Kou, W.; Chen, H.; Wang, W.; Zhang, X.; Guo, T. Sensitivity-Enhanced Extrinsic Fabry–Perot Interferometric Fiber-Optic Microcavity Strain Sensor. *Sensors (Switzerland)* **2019**, *19*, 1–11, doi:10.3390/s19194097.
12. Chen, Y.; Luo, J.; Liu, S.; Zou, M.; Lu, S.; Yang, Y.; Liao, C.; Wang, Y. A High-Strength Strain Sensor Based on a Reshaped Micro-Air-Cavity. *Sensors (Switzerland)* **2020**, *20*, 1–8, doi:10.3390/s20164530.
13. Claes, T.; Bogaerts, W.; Bienstman, P. Experimental Characterization of a Silicon Photonic Biosensor Consisting of Two Cascaded Ring Resonators Based on the Vernier-Effect and Introduction of a Curve Fitting Method for an Improved Detection Limit. *Opt. Express* **2010**, *18*, 22747, doi:10.1364/oe.18.022747.
14. Liu, S.; Wang, Y.; Liao, C.; Wang, G.; Li, Z.; Wang, Q.; Zhou, J. High-Sensitivity Strain Sensor Based on in-Fiber Improved Fabry – Perot Interferometer. **2014**, *39*, 2121–2124.
15. Fabry, C.; Interferometers, P.; Abbas, L.G. Vernier Effect-Based Strain Sensor With Cascaded Fabry–Perot Interferometers. *IEEE Sens. J.* **2020**, *20*, 9196–9201.
16. Nan, T.; Liu, B.; Wu, Y.; Wang, J.; Mao, Y.; Zhao, L.; Sun, T.; Wang, J. Ultrasensitive Strain Sensor Based on Vernier- Effect Improved Parallel Structured Fiber-Optic Fabry-Perot Interferometer. *Opt. Express* **2019**, *27*, 17239, doi:10.1364/oe.27.017239.
17. Gomes, A.D.; Ferreira, M.S.; Bierlich, J.; Kobelke, J.; Rothhardt, M.; Bartelt, H.; Frazão, O. Optical Harmonic Vernier Effect: A New Tool for High Performance Interferometric Fibre Sensors. *Sensors (Switzerland)* **2019**, *19*, 1–18, doi:10.3390/s19245431.
18. Wu, Y.; Xia, L.; Li, W.; Xia, J. Highly Sensitive Fabry – Perot Demodulation Based on Coarse Wavelength Sampling and Vernier Effect. **2019**, *31*, 487–490.
19. Zhang, P.; Tang, M.; Gao, F.; Zhu, B.; Fu, S.; Ouyang, J.; Shum, P.P.; Liu, D. Cascaded Fiber-Optic Fabry-Perot Interferometers with Vernier Effect for Highly Sensitive Measurement of Axial Strain and Magnetic Field. **2014**, *22*, 19581–19588,

doi:10.1364/OE.22.019581.